Reactive laser annealing of indium tin oxide: implications to crystal structure, defect composition, and plasma energy

HILLIER, James Arthur <http://orcid.org/0000-0002-3784-9337>, PATSALAS, Panos, KARFARDIS, Dimitrios, CRANTON, Wayne <http://orcid.org/0000-0002-0142-7810>, NABOK, Alexi V, MELLOR, Christopher J, KOUTSOGEORGIS, Demosthenes C and KALFAGIANNIS, Nikolaos

Research Article | Vol. 12, No. 11 / 1 Nov 2022 / Optical Materials Express 4310
Optical Materials EXPRESS

Reactive laser annealing of indium tin oxide: implications to crystal structure, defect composition, and plasma energy

JAMES ARTHUR HILLIER,[1] PANOS PATSALAS,[2] DIMITRIOS KARFARDIS,[2] WAYNE CRANTON,[3] ALEXI V. NABOK,[3] CHRISTOPHER J. MELLOR,[4] DEMOSTHENES C. KOUTSOGEORGIS,[1] AND NIKOLAOS KALFAGIANNIS[1,*]

[1]School of Science and Technology, Nottingham Trent University, Nottingham, NG11 8NS, UK
[2]Department of Physics, Aristotle University of Thessaloniki, Thessaloniki, GR-54124, Greece
[3]Materials and Engineering Research Institute, Sheffield Hallam University, Sheffield, S1 1WB, UK
[4]School of Physics and Astronomy, The University of Nottingham, Nottingham, NG7 2RD, UK
*nikolaos.kalfagiannis@ntu.ac.uk

Abstract: The mechanisms governing the modification of the optoelectronic properties of low carrier concentration indium tin oxide (ITO) during reactive laser annealing (ReLaA) are investigated. ReLA combines the advantages of reactive ambient thermal annealing and laser annealing; utilizing laser processing of room-temperature sputtered ITO thin films in pressurized reactive environments to probe the films' crystal structure and defect composition. Advanced ellipsometric modelling (considering depth-inhomogeneity and intra- and inter-grain carrier transport), cross-sectional transmission electron microscopy, and X-ray photoelectron spectroscopy revealed ReLA-induced depth-dependent compositional and structural modifications that tuned the carrier concentration ($(0.3-1.27)\times10^{20}$ cm^{-3}) and epsilon-near-zero domain (3.07 – 11.7 μm) across a wider range than previously reported.

1. Introduction

Transparent conductive oxides (TCOs) are appealing materials for a vast suite of optoelectronic applications [1–3]. In recent years, TCOs have also emerged as increasingly favorable materials for plasmonic and active photonic devices because of their unique epsilon-near-zero (ENZ) effect in the near-infrared (NIR) [4]. Specifically, TCOs exhibit strong optical nonlinearities, such as extreme nonlinear dispersion and enhanced light-matter interactions [5]. From these properties arise potential applications of TCOs as epsilon-near-zero materials in optical communications and optical data processing [6]. An important additional asset of TCOs is that their optoelectronic properties can be modulated by engineering their defects, often through a post-growth annealing step [7–10]. This can allow for modulation of the carrier concentration, plasma energy, and thus the ENZ region, further into the mid-infrared (MIR) to target the chemical and biological sensing windows [11–14]. Control and optimization of this adjustment is, however, a complex design problem. We seek to address this challenge by establishing a novel high-throughput method of 'reactive' laser annealing (ReLA) to selectively tune the carrier concentration of tin-doped indium oxide (ITO) thin films, and thus the plasma energy and ENZ domain. In this way, one can ensure the lowest electronic losses and, subsequently, more desirable "figures of merit" (FoMs) for applications within the desired frequency window of operation [15–20].

The most common techniques for annealing of TCOs are indirect annealing techniques such as conventional furnace heating and rapid thermal annealing [21–23]. However, in recent decades the remarkable capabilities of more "direct" annealing techniques, such as laser annealing (LA), to improve the optoelectronic properties of TCOs have become increasingly apparent [24]. Vitally,

#464918 https://doi.org/10.1364/OME.464918
Journal © 2022 Received 1 Jun 2022; revised 21 Aug 2022; accepted 22 Aug 2022; published 13 Oct 2022

Optical Materials EXPRESS

the use of high energy lasers, such as excimer lasers, allows for an ultra-fast (few ns) annealing process that can match the high thermal energy demand of metal-oxides, while the thermal dose is spatially localized, allowing for micro-patterning of the annealed areas as well as the use of heat sensitive substrates [24]. The use of reactive environments during LA has recently been revealed to induce a purely compositionally driven modulation of the optoelectronic properties of ITO thin films, where laser processing within reducing and oxidizing environments of 5%H_2 in N_2 and 100% O_2 promoted an ambient-dependent enhancement of the carrier concentration and mobility, tuning the ENZ region closer to the telecom wavelength (from 1.91 μm to 1.73 μm) [25,26]. To expand the operational window of ITO as a "low-loss" plasmonic and/or photonic material component across the mid-infrared (MIR) spectral window [2,10,13], a strategy to reduce the carrier concentration of ITO *via* ReLA was noted to be of upmost importance [25,26].

In this work, we follow up the foundational demonstration of ReLA [25,26] by exploring the alternative strategy of starting from an "un-optimized" seed, room temperature, sputtered ITO film, purposely grown to possess a high resistivity ($\sim 7 \times 10^{-3}$ Ωcm) and low carrier concentration ($\sim 6 \times 10^{19}$ cm^{-3}). We give special focus onto how the starting film conditions affect the ReLA process by comparing the results to those of our previous work [25]. To elucidate the precise mechanisms behind ReLA, the modifications of the optical and electronic properties were related to changes in the structural and compositional properties. By carefully considering the interplay between the compositional alterations and crystal structure changes, we revealed the influence of both the intra-grain and inter-grain carrier transport properties on the optoelectronic properties of ITO. Depth-dependent, combined structural and compositional changes were uncovered *via* a combination of advanced ellipsometric modelling, X-ray diffractometry, X-ray photoelectron spectroscopy, and cross-sectional transmission electron microscopy. The upper portion of the processed film was subject to a significant enhancement (~×10) of the carrier concentration that could be tuned by controlling both the laser fluence and the oxygen partial pressure of the reactive environment.

2. Experimental details

2.1. Thin film deposition

~130 nm ITO thin films were deposited onto double side polished n-type (1 – 10 Ωcm), 4″, (100) oriented Si wafers with a 2 nm native oxide using radio frequency magnetron sputtering. The seed ITO thin film was deposited with a set of sputtering conditions (power and pressure of 20 W and 5 mTorr., respectively) that were found to produce a lower quality material with resistivity being a magnitude greater than the film produced with optimized sputtering conditions [26] (investigation of the sputtering parameters can be found in Supplement 1, section 1) [25]. The base pressure was $\sim 10^{-5}$ Pa ($\sim 10^{-7}$mbar). Intentional substrate heating or bias was not applied to the substrate. We used a 3″ target of 10 wt.% Sn:In_2O_3 (99.99% purity). Ar and O_2 we introduced to the chamber with an O_2 concentration of 0.25 ± 0.02%. The substrate to target distance was 10.8 ± 0.2 cm. Further details on the deposition process can be found elsewhere [27]. Following deposition, the seed material was diced into $\sim(8 \times 8)$ mm^2 "die".

2.2. Reactive laser annealing

Laser processing was performed at room temperature with a KrF (248 nm) excimer laser (LAMBDA PHYSIK LPX 305i), which delivers unpolarized light at a 1–50 Hz pulse repetition rate and ~25 ns pulse length to the sample surface. Further details of the LA system are published elsewhere [27]. A pressure cell with a UV-transparent window was used to perform the laser processing within pressurized (6.89×10^5 Pa or 100 psig) environments of 5% H_2 in N_2 and 100% O_2. For each ambient composition, a single laser pulse was delivered to the sample with a fluence, J_L, of 25–125 $mJcm^{-2}$ in steps of 25 $mJcm^{-2}$. The beam delivery path can produce a minimum

Optical Materials EXPRESS

spot size of $\sim 3 \times 3$ μm^2, although in this work a spot size of (1.20 × 1.20) cm^2 was used. We note that to achieve a spot size of >1 cm^2 (large enough to enable reliable characterization), 125 mJcm^{-2} was the largest achievable fluence. The fact that the laser spot size was larger than the die also ensured that the entire area of the die was uniformly laser processed.

2.3. Thin film characterization

Optical characterization *via* the measurement of the ellipsometric angles Ψ(E) and Δ(E) was performed using a J. A. Woollam Mark II IR-SE in the spectral range of 0.034–0.8 eV (1.455 – 36.45 μm) and a J. A. Woollam M2000 SE in the spectral range of 0.74–3.34 eV (0.37–1.67μm) at incident angles of 65°, 70°, and 75°. The J. A. Woollam Mark II IR-SE and a normal-incidence optical reflectance probe were also utilized to measure the IR transmittance, $T_{IR}(E)$, and visible reflectance, $R_{Vis}(E)$, respectively. Using the known sample geometry (ITO / 2.63 nm-SiO_2 / Si), an optical model comprising the complex permittivity, $\tilde{\varepsilon}(E)$, of each layer was fit to the full suite of optical measurements (Ψ(E), Δ(E), $T_{IR}(E)$, and $R_{Vis}(E)$). By fitting all measurements simultaneously, we reduce the correlation between the fitting parameters to improve the confidence in the uniqueness and physical reality of the extracted values (see Supplement 1, section 3). From the fitting process, we extract the geometric features (film thickness, surface roughness and uniformity) and optoelectronic properties (interband transitions, phonon modes and/or defect states absorption, free carriers *etc.*) of the ITO films [28]. Electrical characterization was performed *via* four-point probe (4pp) in both collinear and Van-der-Pauw configuration (ρ_{4pp} and ρ_{Hall}). Characterization of the "Hall" carrier concentration, N_{Hall}, was performed with an Ecopia HMS-3000 Hall Measurement System (B = 0.553T) at room temperature.

Structural characterization was performed by XRD employing a PanAnalytical Pro Diffractometer. The spot size was set to 5×5 mm using a 10 mm height-limiting slit, 2^{rad} soller slits, and a programmable divergence slit. The scan step size was 0.0083556° with a time per step of 1998.345 *s* in a range of 25° – 40°. The long step time was required due to the small sample footprint and the amorphous nature of the as-grown ITO films. The range was chosen to cover the most clearly identifiable (222) and (400) Bragg peaks for bixbyite In_2O_3, at 30.6° and 35.5°, respectively [29]. Cross-sectional images of an indicative set of ITO thin films were obtained *via* high resolution TEM (FEI Talos S/TEM) using a Schottky-type field emission gun operated with an electrostatic potential of 200 kV. Prior to TEM, the films were subjected to focused ion beam milling process using a JEOL 4500 FIB/SEM. Surface elemental characterization was performed with a Kratos Analytical Ltd. AXIS Ultra XPS system using a monochromated Al-$K_{\alpha 1}$ X-ray beam excitation source (1486.6 eV) in an ultra-high vacuum chamber (base pressure ~10^{-9} bar). The relative elemental abundance across the entire depth of the ITO thin films was determined from EDX measurements with the FEI Talos S/TEM.

3. Spectroscopic Investigation of the seed and laser processed films

3.1. Optical modelling

To reveal the optoelectronic properties of the seed ITO films and those subjected to ReLA we firstly look at the optoelectronic properties, which define the key characteristics of TCOs that are associated with most applications [1,30]. Figure 1(a) presents Ψ(E) (blue squares) and Δ(E). (red squares) of an indicative seed ITO thin film (see Supplement 1, section 2 for optical measurements of all samples). The solid green lines show the best fit across the entire spectral range. We note the more complicated line-shape of Ψ(E). and Δ(E). as compared to the higher-quality (lower resistivity) ITO film deposited with optimized deposition conditions (Supplement 1, Fig. S3) [25]. To fit Ψ(E) and Δ(E). of the seed and laser processed ITO films we need to consider a more-complex inhogeneity than has been previously reported for high-quality ITO films [25,31–33]. It is vital to note that by appending $T_{IR}(E)$ to Ψ(E) and Δ(E) during the

Optical Materials EXPRESS

fit, we were ato exclude the presence of additional IR oscillators to explain the complex line shape of $\Psi(E)$ and $\Delta(E)$. A detailed description of this process and a justification of the utilized model is presented in Supplement 1, section 3. Briefly, the ITO film is separated into two distinct layers: a "top" and "bottomlayer, where the top layer comprises most of the film. Each layer is described by a complex permittivity, $\tilde{\varepsilon}(E)$. The imaginary part of the complex permittivity, $\varepsilon_2(E)$, is described by a summation of multiple oscillators (Eq. (1)) and the real part of the complex permittivity, $\varepsilon_1(E)$, is derived from a Kramers-Kronig transformation of $\varepsilon_2(E)$ with a background contribution to the permittivity, ε_∞ [31,34].

$$\tilde{\varepsilon}(E) = \varepsilon_1(E) + i\varepsilon_2(E) = \varepsilon_\infty + \sum_{s=1}^{S} \frac{-\hbar^2 e^2 N_{opt,s}}{\varepsilon_o \left(m_e m^* E^2 + i \left(\frac{e\hbar}{\mu_{opt,s}} \right) E \right)} + \sum_{m=1}^{M} \tilde{\varepsilon}_m(E), \quad (1)$$

where $\hbar$ is the reduced Plank's constant (in eVs) and ε_o is the vacuum permittivity. e, m_e and m^* are the charge, mass, and effective mass ratio of the free carrier (electron). The second term describes a summation of multiple Drude terms that represent distinct carrier species [35], a consideration that has been taken for materials suspected of containing various charge carriers such as holes and electrons, light and heavy holes, and/or electrons in different conduction band valleys [35]. $N_{opt,s}$ and $\mu_{opt,s}$ are the "optical" carrier concentration and mobility, respectively, for the s^{th} carrier species. The choice to express Eq. (1) in terms of N_{opt}, μ_{opt}, and m_e (instead of resistivity and mean time between collisions) will become apparent in the discussion below. The third term describes a summation of multiple oscillators that describe phonon, defect and/or interband absorption. In total, the ITO film comprised one Tauc-Lorentz [34], two Gaussian and two Drude oscillators. Further information regarding the analytical apparatus alongside the formulation of each oscillator is given in Supplement 1, section 3.

Figure 1(b) presents ε_2 (solid red line), and the individual components which make up $\varepsilon_2(E)$ (dashed lines), for the top layer of the seed ITO film. The optical constants for all seed and laser processed films (alongside tabulated lists of all the corresponding fitting parameters) can be found in Supplement 1, section 2. The two IR Gaussian peaks are shown as the cyan and pink dashed lines. The multiple phonon peaks of ITO between 0.03 eV and 0.07 eV [36] cannot be individually resolved and so are represented here by a single Gaussian oscillator (dashed cyan line). The 2^{nd} Gaussian oscillator, at ~0.15 eV (dashed pink line), is either a phonon peak due to hydroxides [37] or a potential defect state [25]. The purple dashed line shows the tail of the UV absorption, described by a Tauc-Lorentz oscillator (dashed purple line), centered at 3.93 eV [37]. The most significant contribution to the optical absorption in the IR comes from the free carriers. For detailed electrodynamic analysis, the free carrier absorption is described here with two Drude terms (2^{nd} term in Eq. (1); dashed orange and green lines in Fig. 1(b). The requirement of two Drude terms to achieve a good fit suggests that, in the top layer, there exist two "carrier species" with independent $N_{opt,s}$, $\mu_{opt,s}$ and $m^*_{e,s}$ (i.e., $N_{opt,t1}$, $N_{opt,t2}$, $\mu_{opt,t1}$, $\mu_{opt,t2}$, $m^*_{e,t1}$, and $m^*_{e,t2}$; where the subscript t denotes that the species resides within the top layer). The two carrier species reflect different routes for carrier transport within the ITO layer, the mechanisms for which will be discussed below.

Figure 1(c) presents $\varepsilon_2(E)$ for the bottom layer of the seed ITO film (solid red line). The bottom ITO layer is described using a gradient between the carrier concentration at the ITO/SiO_2 interface, $N_{opt,b}$, and within the top layer, $N_{opt,t}$. The overall steepness of the gradient is defined by the layer height, d_b. The shape approximates an exponential gradient [38]. This layer comprises 20 individual sub-layers of discrete $N_{opt,z}$, $\mu_{opt,z}$ $m^*_{e,z}$ and $T_{G,z}$, where the subscript z denotes that the parameter is defined at a distance $d_B z/20$ from the ITO/SiO_2 interface. We formulate the Drude terms within Eq. (1) using $N_{opt,s}$ and $\mu_{opt,s}$ (here forth referred to as "the transport properties") as the gradient is more physically represented by variations in the transport properties than in the optical resistivity, ρ_{opt}, and mean time between collisions, τ_{opt}. This also enables us

Optical Materials EXPRESS

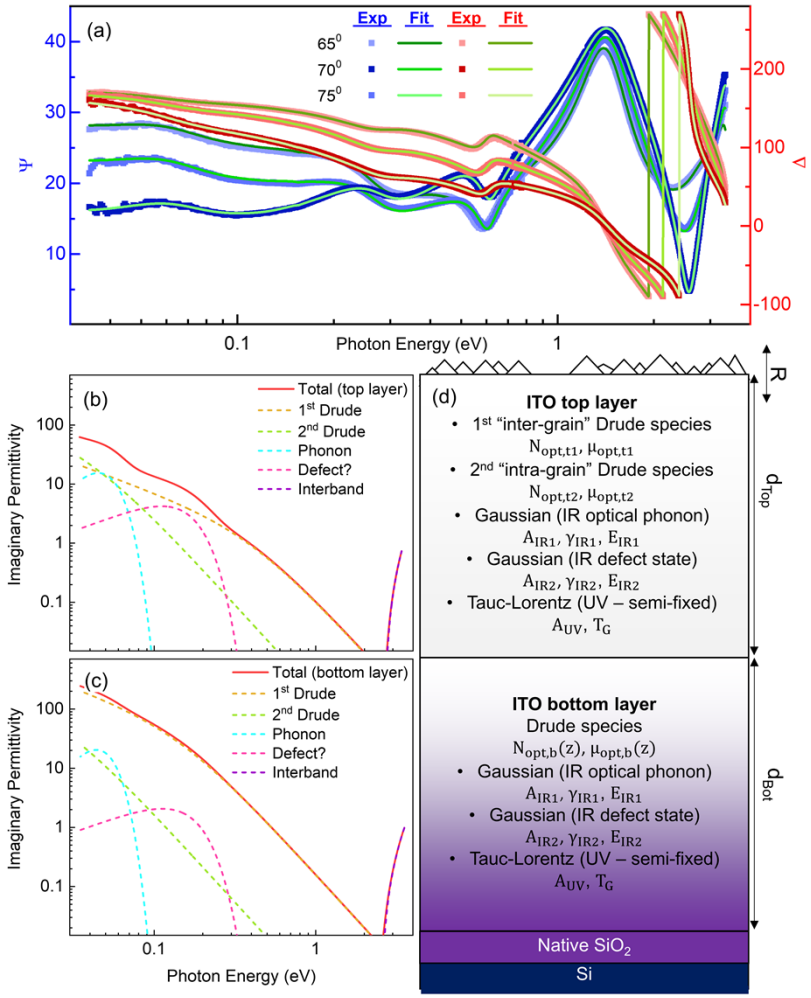

Fig. 1. (a) Measured Ψ(E) (blue squares) and Δ(E) (red squares) the seed ITO thin film alongside the corresponding fit (green lines). (b-c) The fitted imaginary permittivity for the (b) top and (c) bottom layers of the seed ITO thin film (solid red line) with the individual components of the imaginary permittivity for the 1st (dashed orange line) and 2nd (dashed green line) free carrier species, phonon (dashed cyan line), potential defect state (dashed pink line), and interband transition (dashed purple line). Logarithmic scales in the x- and y-axes are used in (a-c) to exaggerate the IR spectral region. (d) Schematic of the multi-layer geometric and parametrized optoelectronic model.

Optical Materials EXPRESS

to consider the non-parabolicity of the conduction band due to free carrier population [39] to describe $m^*_{e,n}$ as a function of $N_{opt,n}$ throughout the sample depth. We also allow the Tauc-Gap, T_G, [34] to vary with depth, reflecting the potential Burstein-Moss shift with changing carrier concentration [40]. This improves the fit in the visible range. All other parameters are left free during the fit but do not vary with depth (i.e., they are identical for the top and bottom layer). Finally, we follow the suggestions of previous reports [31,33] and include a layer of surface roughness described by an effective medium approximation of 50% of the top layer and 50% air. Altogether, these steps ensure that the optical model accurately reflects reality.

As discussed, there exist three independent carrier species that define the optical carrier transport properties across the sample depth of the ITO film. This inevitably makes it difficult to extract useful information about how the optoelectronic properties of the low-N seed ITO films are affected by ReLA. To aid in this matter, it is helpful to note that N and μ are linked through the influence of scattering mechanisms. The precise nature of this interdependence of the transport properties has been described for the case of ITO [41,42]. The formulation of the "scattering equation" that defines μ(N) by considering each scattering mechanism in turn, is detailed elsewhere [32]. Therefore, to see the full picture of the transport properties of each seed and laser processed film, we compare the transport properties for the 1st and 2nd top-layer species in Fig. 2. The case for the bottom layer and a comparison of optical and electrical results is presented within Supplement 1, section 3 (Fig. S21). Due to the complexity introduced by the existence of multiple species of carriers across the film, the analysis requires careful, step-by-step, examination before summarizing the overall picture. Firstly, we examine the seed films (and those annealed at "low" fluences) to elucidate the identity of the two carrier species in the top layer. Then we examine how ReLA at higher fluences affects each layer and carrier species. Finally, we compare the results with those for the bottom layer and Hall Effect values of the transport properties.

3.2. Dual carrier species of ITO

Figure 2 presents μ_{opt} against N_{opt} for the 1st (darker shaded symbols) and 2nd (lighter shaded symbols) carrier species that exist within the top layer of the seed ITO films (grey stars) and those subject to single-pulse ReLA at 25–125 mJcm^{-2} in 5% H_2 in N_2 (red squares) and 100% O_2 (green triangles). The labels indicate the fluence used during laser processing and are colored red or green for annealing in 5% H_2 in N_2 or 100% O_2, respectively. For comparison, the case for seed and laser processed ITO films that were deposited with optimized deposition conditions [25] are presented with the open symbols.

We indicate multiple theoretical trends of μ(N) with the dashed lines, where the parameters defining the trend are fit to particular "clusters" of data. Subsequently, it is found that each cluster relates to a set of samples where the scattering mechanisms that influence μ_{opt} in relation to N_{opt} are the same. The fits of μ(N) to each cluster are indicated with the purple, orange, pink, and blue dashed lines. The first cluster (indicated by the gold shaded area) represents the 1st carrier species within the top layers of the seed ITO films and those subject to ReLA at fluences of 25 – 100 mJcm^{-2}. We immediately notice the significantly lower N_{opt} in comparison to previous reports for "optimized" (lower resistivity) ITO films [25,31–33], which is the primary source of the larger ρ_{opt} for the ITO films of this work. For this cluster of samples, we observe that μ_{opt} increases with N_{opt}. This indicates that, in this case, grain boundary scattering (GBS) is the dominant scattering mechanism [42]. We indicate the trend of μ(N) fit to the 1st cluster with the dashed gold line. Within the small range of N covered by this cluster, only the parameters relating to the effect of GBS and ionized impurity scattering (IIS) matter (due to Matthiessen's rule). Therefore, only the grain size, L, and trap density, Q_t, were left free during the fit of the scattering equation [41,42] to the data, and were determined to be 2.0 ± 0.2 nm and (7.0 ± 0.3)×10^{12} cm^{-2}, respectively. The fine grain size indicates that the film is nanocrystalline/amorphous. The other

Optical Materials EXPRESS

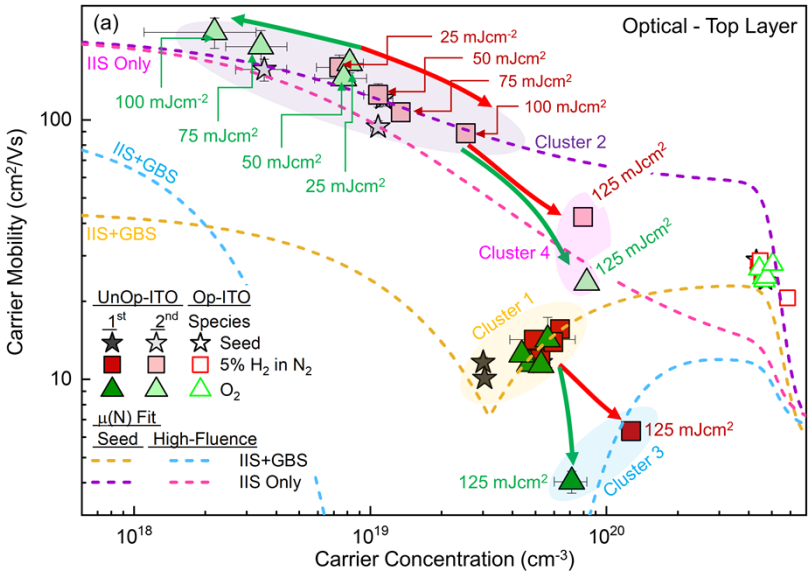

Fig. 2. Optical, "top layer", carrier concentration, $N_{opt,ts}$, and mobility, $\mu_{opt,ts}$, of the seed ITO thin films (grey stars) and those subject to single-pulse ReLA at 25 – 125 mJcm^{-2} in 5% H_2 in N_2 (red squares) and 100% O_2 (green triangles). The 1st and 2nd carrier species are denoted by a dark and light symbol color, respectively. For easy comparison, we also present the corresponding transport mechanisms for seed and laser processed ITO films that were deposited with optimized deposition conditions, taken from [25]. The dashed lines indicate the theoretical trends of μ(N) from various scattering mechanisms. The parameters of $\mu(N)_{IIS+GBS}$ that are related to grain boundary scattering (grain size, L, and trap density, Q_t) are fit to the 1st carrier species within the seed materials and those subject to ReLA at ≤ 100 mJcm^{-2} (gold dashed line) and at 125 mJcm^{-2} (cyan dashed line). The corresponding $\mu(N)_{IIS}$ relation, which ignores the effect of grain boundary scattering, for the films annealed at 100 mJcm^{-2} and 12 mJcm^{-2} are indicated by the purple and pink dashed lines, respectively. The green and red arrows indicate ambient dependent transitions in carrier concentration after ReLA in 5% H_2 in N_2 and 100% O_2, respectively.

parameters were fixed to previously reported values [42] or (for the IIS-diminished mobility, μ_{IIS}, and the coefficient of ionized cluster scattering (ICS), α_{ICS}) to those fit to previous results for a set of optimized ITO films [32].

The second cluster (purple shaded area in Fig. 2) represents the 2nd carrier species (lighter shaded symbols) within the top layer of the seed ITO films and those subject to ReLA at 25 – 100 mJcm^{-2}. The second cluster has considerably (approximately a factor of 10) lower N_{opt} and larger μ_{opt} than the first cluster. There is a negative trend of μ(N) that is equivalent to the trend of μ(N) for the first species, if only the influence of GBS is ignored (i.e., μ(N) is not fit to this cluster but arises simply by removing the contribution of GBS to the scattering equation). We show this with the dashed purple line in Fig. 2. Indeed, the values of μ(N) for the 2nd species agree well with those for epitaxial films of In_2O_3 and ITO [43–45]. From this observation, we can formulate an understanding of the physical mechanism behind the existence of two charge species within the top layer. Specifically, the first species experiences the influence of GBS whereas the 2nd species does not. Therefore, the 1st species can be explained as the free carriers which oscillate in response to the driving electromagnetic field across grain boundaries. Conversely, the 2nd species oscillates within the individual grains. To further validate this claim, we consider that due to the nanocrystalline nature of the room-temperature deposited ITO films,

Optical Materials EXPRESS

the grains can be smaller than the mean free path, $l_{e,IIS}(N)$, that is calculated by considering the effect of IIS using the degenerate electron gas model [46,47],

$$l_{e,IIS}(N) = v_f(N)\tau_{opt}(N), \tag{2}$$

where v_F is the Fermi velocity, given by:

$$v_F(N) = (3\pi^2)^{\frac{1}{3}} \left(\frac{\hbar}{m_e^*(N)}\right) N^{\frac{1}{3}}. \tag{3}$$

This gives values of $l_{e,IIS}(N) = 3.9 - 5.5$ nm for $N = 10^{18} - 2.7 \times 10^{19}$ cm^{-3} (the N-range of the 2nd cluster). Vitally, these values for $l_{e,IIS}(N)$ are larger than L, suggesting these carriers should not scatter within the grain. It should, however, be noted that the scattering events which give rise to $l_{e,IIS}(N)$ are, inherently, statistical phenomena. Even if $l_{e,IIS}$>L, a fraction of the carriers will be scattered off ionized impurities before the grain boundaries and another fraction will be scattered within the grain boundaries. The "transmitted" fraction of carriers, $T_{N,IIS}$, (i.e., those that make it to the grain boundaries) can be described by:

$$T_{N,IIS} = \frac{N_{IIS}}{N} = e^{-L/l_{e,IIS}}, \tag{4}$$

where N_{IIS} is the number of free carriers that make it to a grain boundary. From Eq. (4) it is calculated that, across the N-range covered by the 2nd carrier species within the seed films, $T_{N,IIS} = 67\% - 69\%$. In other words, 31% – 33% of the free carriers will experience only IIS. For the seed films, the population of the 2nd carrier species is 11.7% – 36% of the total free carrier population. The lower (though overlapping) range of values for the 2nd carrier species population likely arises from the distribution of L within each film, where the average grain size, $\bar{L}$, is weighted by many small grains and fewer larger grains [48]. These results build confidence that the 1st carrier species describes the free carriers that scatter off grain boundaries and that the 2nd carrier species described those that scatter off ionized impurities within the grains. Therefore, here forth the 1st and 2nd carrier species are designated as the "inter-grain" and "intra-grain" carriers, respectively. It is also important to note that because L is so small, the picture of distinct grains with sharp grain boundaries may be misleading as the conductivity of nanocrystalline TCOs arises from the direct overlap of large and non-directional metal atom s-states [49,50]. This suggest that GBS would play a minor role in the conduction mechanisms for nanocrystalline ITO. However, in Fig. 2, and elsewhere [32], it is seen that the modelling of μ(N) with Seto's model of GBS [51] is empirically sufficient to fit the trend of the experimental films. Therefore, instead of sharp grain boundaries where the crystal orientation of distinct grain changes, the amorphous film likely comprises localized regions of carrier traps, where the carriers around the traps are depleted. The result is that the carrier mobility through the film is affected in a similar fashion to GBS. The localized carrier traps may arise from neutral clusters of $(SnO_2)_2$ where the additional oxygen atoms play the role of electron traps [52] Alternatively, the two species may arise from carrier transport across the metal 5s and the oxygen p-orbitals, respectively, in a way that is analogous to the dual-carrier species observed across different molecular chains in polymers [53]. As the physical mechanism behind the empirical adherence to Seto's model is currently unidentified, the nomenclature of grains and grain boundaries will continue to be used in this work. To the best of our knowledge, this is the first demonstration of an optical model able to distinguish between intra- and inter-grain transport. The utilization of IR SE with advanced optical modelling (examined in terms of the scattering mechanisms), may be applicable to a wide range of nano- and poly-crystalline materials.

3.3. Effect of ReLA

The third and fourth clusters (light blue and pink shaded areas in Fig. 2, respectively) represent transitions to different "branches" of μ(N) brought on by ReLA at 125 mJcm^{-2}. The population

Optical Materials EXPRESS

density for the intra-grain carriers is greatly increased, into the order of the inter-grain carriers. This indicates that the number of high mobility conduction pathways have increased, possibly by breaking up the neutral clusters of $(SnO_2)_2$. We fit $\mu(N)$ to the 3rd and 4th clusters simultaneously with $\mu(N)$ considering either only IIS (dashed pink line in Fig. 2) or IIS + GBS (dashed cyan line in Fig. 2). To do so, μ_{IIS} and Q_t are required to be free parameters. Due to the limited sample set, we are required to fix L at 6nm (determined by XRD; see Fig. 3) to avoid over-correlation of the free parameters. μ_{IIS} and Q_t are subsequently determined to be 10 ± 4 cm^2/Vs, and $(18.2 \pm 0.3) \times 10^{12}$ cm^{-2}, respectively. This represents a decrease in the IIS/lattice limited mobility and an increase in both the grain size and trap density after laser processing at 125 mJcm^{-2}. This is indicative of a transition of the structure to one that contains more distinct and crystallized granular phases, with higher grain boundary potentials, dispersed within the amorphous phase [54]. The lower value of μ_{IIS} also infers an increased concentration of ionized impurities (activated Sn or oxygen vacancies; to be explored further below). For both the 1st and 2nd carrier species, the samples annealed in 5% H_2 in N_2 tend to show larger values of N_{opt} than for those annealed in 100% O_2. Indeed, we note a decrease in N_{opt} with increasing fluence for ReLA in 100% O_2. We indicate this with the red and green arrows in Fig. 2.

To the best of our knowledge, this is the first time that ReLA in oxidizing environments can reduce the carrier concentration of ITO. This has profound implications for the field of plasmonics, as ReLA can be used to tune the plasma energy of ITO further into the IR, increasing the operational window for "low-loss" plasmonics [13,55,56]. An indicative set of 'figures of merit' (FoMs) (for surface plasmon resonance (SPR) [16], localized SPR (LSPR) [16], near-field enhancement [15], and photothermal conversion [15]) are given in Fig. S16 in Supplement 1, section 2 and demonstrates how ReLA can both enhance the peak values of each FoM and expand the range of negative permittivity where plasmonic effects can be exploited. Finally, examination of the 1st carrier species within the film annealed at 125 mJcm^{-2} reveals, again, an ambient dependence to the increase in N_{opt}, where there is greater enhancement for the reducing environment. For the bottom layer, N_{opt} is significantly higher than in the top layer and is largely unaffected by ReLA due to the depth-dependence of the thermal treatment (see Supplement 1, section 3).

In summary, the optoelectronic properties of the studied seed ITO film grown with "un-optimized" sputtering conditions are far more complex than observed during previous reports of ReLA of high-quality ITO films [25]. The seed film has an inherent inhomogeneity (described by a gradient in the carrier transport properties) and multiple carrier species (due to "inter-grain" and "intra-grain" carrier species). To the best of our knowledge, this is the first observation of a dual carrier species present in ITO. Only by fitting a complex optical model to the ellipsometric measurements could we accurately extract the carrier transport properties. Furthermore, by investigating the resulting properties through the lens of the various scattering mechanisms at play could the electrical behavior throughout the sample, and the influence of ReLA, be fully elucidated. We revealed the nature of the photo-induced modifications of the optoelectronic properties of the "un-optimized" ITO film, with similar effects as found for the optimized film [25]. We find an ambient-dependent modulation of N at 125 mJcm^{-2}, increased for more reducing environments, and, vitally, find that ReLA in 100% O_2 can reduce the carrier concentration. However, the carrier mobility is reduced. Using previous studies as a guide [25], we have been able to infer some of the underlying physical mechanisms behind the conversion of the optoelectronic properties during ReLA. However, due to the complex nature of the film structure further experimental effort is required to fully elucidate the precise nature of such photo-induced modifications.

Optical Materials EXPRESS

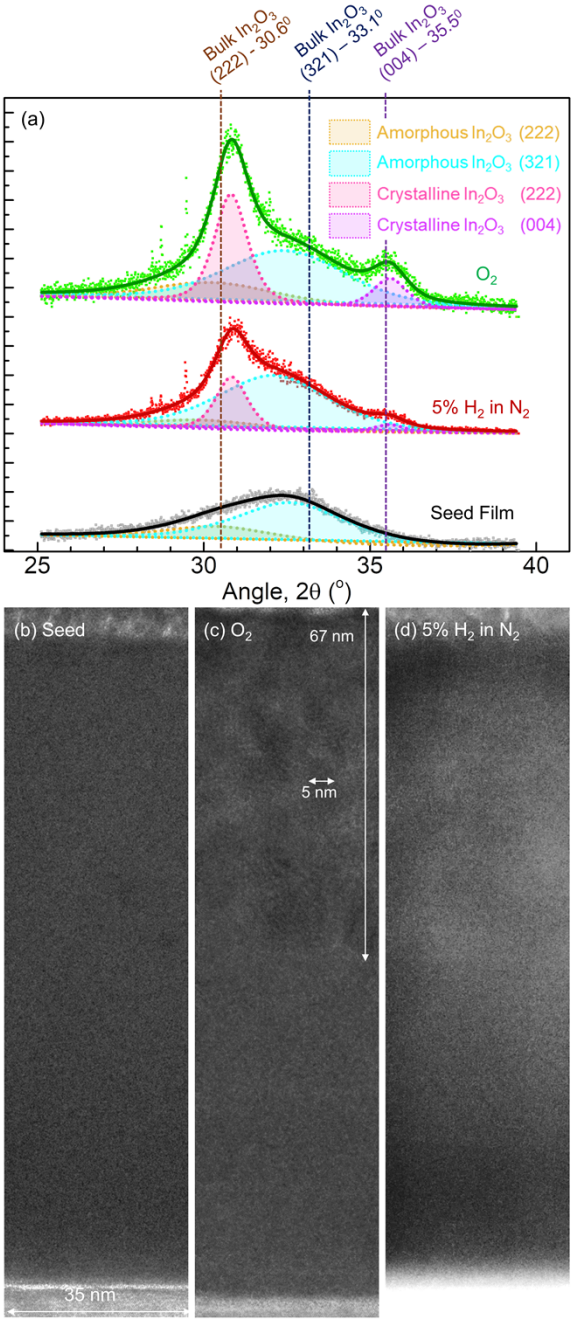

Fig. 3. X-ray diffractograms for the seed ITO film (grey squares) and those subject to ReLA in 5% H_2 in N_2 (red squares) and 100% O_2 (green squares) at 125 mJcm^{-2}. The solid black, red, and green lines represent the corresponding fit of two pseudo-Voigt functions to the data. For the seed film, we present the component peaks, representing regions of the film under tensile and compressive stress, as the gold and cyan dashed lines respectively. For the laser processed films, we present the additional "unstressed" (222) and (400) Bragg peaks as the pink and purple dotted lines, respectively. Also shown are the TEM cross-sectional images of (b) the seed ITO film and those subject to ReLA at 125 mJcm^{-2} in (c) 100% O_2 and (d) 5% H_2 in N_2.

Optical Materials EXPRESS

4. Structural ReLA-induced modifications

To investigate whether ReLA has induced any modifications to the film crystallinity which may elucidate the changes to the optoelectronic properties observed in Fig. 2. The crystal structure of the seed and processed ITO films was studied via XRD. Figure 3(a) presents the X-ray diffractograms for the seed film (grey squares) and the corresponding films processed with a single laser pulse at 125 mJcm^{-2} in 5% H_2 in N_2 (red squares) and in 100% O_2 (green squares). The X-ray diffractograms for all samples can be found in Supplement 1, section 4. The seed film shows a broad, asymmetric peak at centered at ~32.5°. We indicate the (222), (321), and (400) peak positions for crystalline, unstressed In_2O_3 at 30.607°, 33.127°, and 35.49°, respectively [9,29], with the dashed brown and purple lines, respectively.

The diffraction peak is fit with two pseudo-Voigt functions that represent each crystalline orientation, which we indicate these with the gold and cyan dotted lines, respectively. For the films annealed at 125 mJcm^{-2}, two new peaks emerge from the broad asymmetric peak. This indicates that the film now has a semi-crystalline nature [57]. The positions of these peaks more accurately reflect those for an unstressed, crystalline ITO film. Therefore, we note that ReLA has induced crystallization of a portion of the ITO film, and we present the pseudo-Voigt peaks that represent the crystallized (222) and (400) peaks with the pink and purple dotted lines, respectively, in Fig. 3(a). This is confirmed by examining Fig. 3(b)-(d), where we present the TEM cross-sectional images for the seed ITO film and those subject to ReLA at 125 mJcm^{-2} in (c) 100% O_2 and (d) 5% H_2 in N_2. The seed film is highly uniform across the sample depth and no crystallization can be observed. However, for the film annealed at 125 mJcm^{-2} in 100% O_2, a clear region of distinct crystallites is observed within the top ~67 nm of the film. The "fingerprint" like patterns which represent the grains are approximately 5 – 9 nm in diameter.

This region can also be faintly observed for the film annealed in 5% H_2 in N_2, but determination of the crystallite size is inhibited by the lower quality of the image. This observation reveals that the two regions of an amorphous and polycrystalline character observed via XRD corresponds to the top and bottom layers of the film (as described above). The distinct layers arise from the inherent depth-dependence of the ReLA thermal treatment. The existence of a lower, amorphous layer and an upper, polycrystalline layer in the ITO film after ReLA can be ascribed to the heating mechanism of laser annealing [24,25]. The penetration depth, δ_p, (purple line in Fig. 4(a)) for the seed ITO film was calculated to be 43.2 ± 0.1 nm [1]. Within the region defined by δ_p, the heat is predominantly generated by the absorption of the KrF photons. This region is indicated by the purple shaded area in Fig. 4(a). The lower portions of the film are then heated by heat diffusion from the top ~67 nm. The diffusion will also result in an exponential decay of the peak temperature as a function of the depth (Fig. 4(b)). This region is indicated by the red shaded area in Fig. 4(a). Below this region, the temperature increase would be insufficient to significantly affect the material. Depending on the thickness of the film, this threshold may occur within the film, or extend into the substrate itself so that the entire film is thermally affected [24,25]. This region is indicated by the red shaded area in Fig. 4(a). The reduced significance of the thermal annealing further down the film explains why the transport properties only vary by ~±10% for the bottom layer of the laser processed ITO films (see Supplement 1, section 3). In Fig. 3(c)-(d), however, it was seen that the region of polycrystallinity stops at a depth of ~67 nm, which is ~60% larger than the calculated δ_p. The absorption of the photons does not cut-off at the edge of the penetration depth. Instead, there is a smooth exponential gradient of the laser photon intensity (Fig. 4(a)) and thus temperature increase due to photon absorption. Across the film, the difference in the absorption would result in a gradient of the peak temperature reached during the ReLA process.

An illustration of the variation of the peak temperature, T_{Peak}, across the depth of the sample is shown as the solid red line in Fig. 4(b). The peak temperature closely follows the laser photon intensity. For a critical intensity of photons, T_{Peak} would be sufficiently high to induce a

Optical Materials EXPRESS

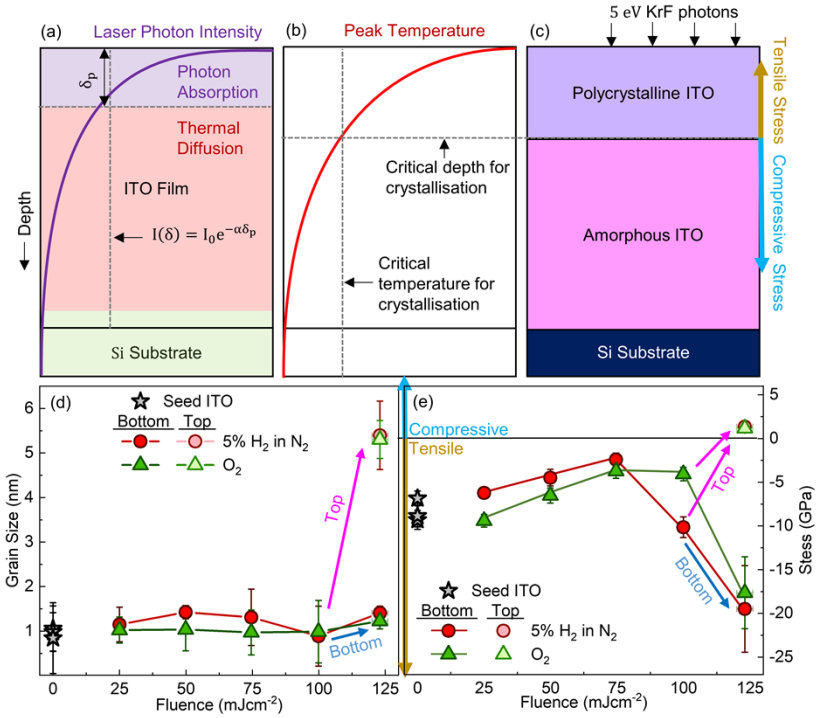

Fig. 4. (a-c) Schematic illustrating the thermal depth-dependence of the ReLA process. Extracted (d) grain size and (e) internal film stress of the seed un-optimized ITO films (grey stars) and those subject to ReLA at 25–125 mJcm^{-2} in 5% H_2 in N_2 (red circles) and O_2 (green triangles). The light shaded symbols denote top layer of the film after ReLA at 125 mJcm^{-2}.

crystallization of the ITO film. An illustrated example T_{Peak} is indicated by the vertical dashed line in Fig. 4(b). Figure 3(c)–(d) demonstrates that this critical temperature must be reached within the upper, polycrystalline region that extends ~67 nm into the film. This region is indicated with the purple slab in Fig. 4(c). Below this region the peak temperature is insufficient to induce crystallinity and the layer remains amorphous. This is indicated with the pink slab in Fig. 4(c). It should be noted that the photon absorption relative to the incident photon intensity (i.e., the laser fluence) as a function of the depth is dependent only on the optical constants and the sample geometry [24,25]. However, the absolute absorption and thus the peak temperature as a function of the depth would depend on the fluence and other properties of the material such as the thermal conductivity and entropy. Furthermore, the critical temperature for the promotion of crystallinity must not only depend on the absorption coefficient at 5 eV.

This can be inferred by how laser processing of an ITO film with optimized sputtering conditions [25] did not show an upper crystallized layer even though the optical constants in the UV (above the band gap) were highly similar [26] (see Supplement 1, section 2). The heating mechanism described above results in a depth-dependent modification of the microstructural and optoelectronic properties. Figure 3(a) showed that the peak position of the (222) ITO peak for the seed ITO film was lower than the bulk (222) peak position of 30.6°. For films annealed at 125 mJcm^{-2}, the (222) peak is split into two parts for both the amorphous and crystalline layers. The peak for the amorphous (bottom) layer exists below the bulk (222) position and thus remains under compressive stress. Conversely, the peak for the crystalline (top) layer exists above the bulk (222) peak position and indicates the top portion of the film is under a tensile stress. The

Optical Materials EXPRESS

change in the crystalline state between the top and bottom layers cautions a direct comparison of the XRD peaks. However, the compressive stress of the seed ITO film and lower region of the laser processed films likely arises from the interfacial mismatch between the atomic spacings of the Si and In_2O_3 lattices [58]. Furthermore, the high oxygen content at the bottom of the seed film (Fig. 5(d)) leads to a stretching of the lattice and a compressive stress, increasing the d-spacing and reducing the Bragg peak position. For the upper layer, the reduction in oxygen and creation of oxygen vacancies significantly reduces the d-spacing, resulting in a tensile stress. We consider it of great interest that the structural modifications occur at 125 $mJcm^{-2}$ for the "un-optimized" ITO film studied in this work but not for an ITO film deposited with optimized sputtering conditions [25]. This is compounded by the observation in our previous work that $\varepsilon_2(E)$ at 5 eV (the KrF excimer laser energy) is lower for the un-optimized (low-N) film than for the optimized (high-N) film [32].

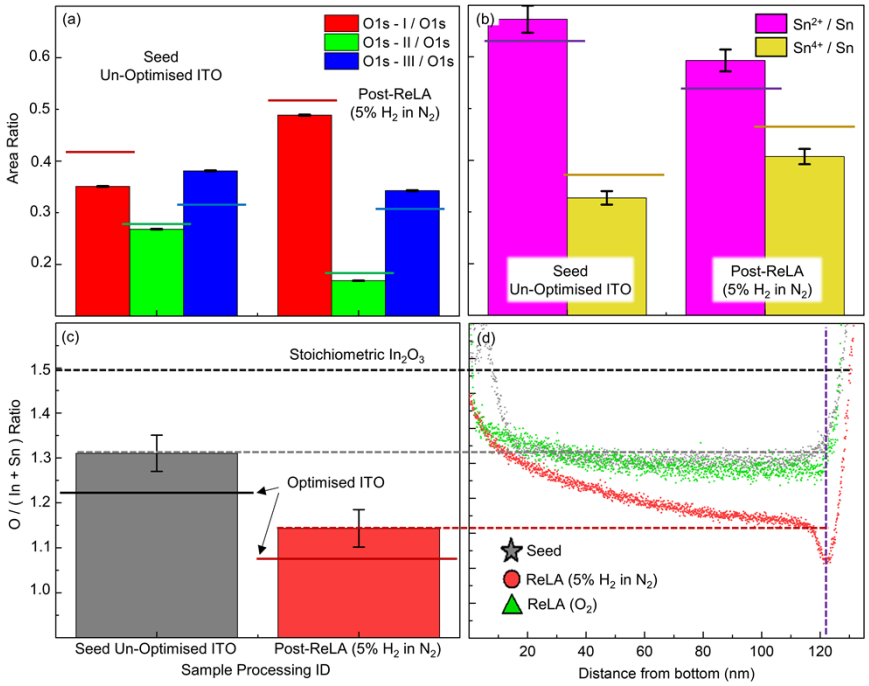

Fig. 5. Relative areal intensities of the deconvoluted component peaks of the core level X-ray photoelectron spectra for (a) O1s peaks: O_I (red bar), O_{II} (green bar) and O_{III} (blue bar) and (b) Sn: Sn^{2+} (pink bar) and Sn^{4+} (yellow bar) for the seed ITO film and that subject to a single ReLA pulse at 125 $mJcm^{-2}$ in 5% H_2 in N_2. (c) The O/(In + Sn) ratio for the seed ITO film (grey bar) and that subject to a single ReLA pulse at 125 $mJcm^{-2}$ in 5% H_2 in N_2 (red bar), calculated from surface-XPS. In (a-c), the solid horizontal lines indicate the values reported for an ITO film, with larger carrier concentration, deposited with "optimized" sputtering conditions. (d) Depth profile of O/(In + Sn) for the seed ITO film (grey stars) and those subject to single ReLA pulse at 125 $mJcm^{-2}$ in 5% H_2 in N_2 (red circles) and 100% O_2 (green stars), calculated from EDX imaging. O/(In + Sn) for stoichiometric In_2O_3 is indicated with the dashed black line. We map the XPS results onto the 'surface' (purple dashed line) of the EDX profile with the grey and red dashed lines.

Optical Materials EXPRESS

We posit two possible causes for the increased "sensitivity" of the un-optimized film to the energy dose:

i. The low thermal conductivity of the film (due to the lower N) results in the thermal energy persisting for longer within the top layer during the rapid annealing, leading to a higher peak temperature for a given fluence [24].

ii. The higher entropy within the un-optimized film results in a more "effective" utilization of the thermal energy for atomic rearrangement.

Indeed, both factors may be at play and thus a deeper theoretical investigation into the heat diffusion mechanisms during ReLA is highly warranted.

In summary, at higher fluences (125 mJcm^{-2}) in both reducing and oxidizing ambient environments, a polycrystalline nature was introduced to the upper layer of the film (with a grain size of 5–9 nm) while the lower layer remained amorphous. The depth of the polycrystalline layer was shown to result on the change in the photon absorption and peak temperature as a function of depth across the film. The depth-dependence of the laser processing explains the minor changes to the bottom of the ITO film during ReLA. However, the modulation of the carrier transport properties observed for the upper layer in Fig. 2 cannot be explained by a change in the structure alone. Furthermore, optical modelling revealed a high depth inhomogeneity in the seed ITO film itself. To explain these observations, an extensive investigation into the compositional properties of the seed and laser processed films was required.

5. Compositional ReLA-induced modifications

To reveal the precise nature of compositional modifications and how they relate to the alterations of optical properties of ITO during laser processing, we examined the surface oxidation states of the individual elements, via XPS, for the seed ITO film and for the ITO film subjected to single-pulse ReLA at 125 mJcm^{-2} in the reducing environment (5% H_2 in N_2). Figure 5(a)-(b) presents the resultant areal intensities of (a) the O_I (red bar), O_{II} (green bar) and O_{III} (blue bar) components of the O1s core-level X-ray photoelectron spectra and (b) the Sn^{4+} (pink bar) and Sn^{2+} (yellow bar) components of the $Sn3d_{5/2}$ core-level X-ray photoelectron spectra . For comparison, the solid horizontal lines of each color presented across each bar indicate the values for an "optimized" ITO film with a larger carrier concentration [25]. Inspection of the deconvoluted O1s peaks reveals that the surface oxidations states for the seed ITO film of this work are different to those of the optimized film. Specifically, in relation to the optimized ITO film: the O_I peak that is related to the metal oxide [59] is significantly decreased while the O_{III} peak, related to surface contaminants [60], is increased. The O_{II} peak, related to oxygen atoms in the amorphous phase of ITO and/or oxygen atoms bound to Sn [60–62], is largely the same. This suggests that the ITO film of this work is highly entropic or amorphous [63], that there is a higher concentration of surface defects related to hydroxides [64], and/or that there is a smaller presence of metallic In [8]. Inspection of the deconvoluted Sn3d peaks for the seed ITO film revealed that the Sn^{4+} states are reduced in comparison to the high-quality ITO films [25], partly explaining the lower values of N_{opt} and N_{Hall} observed in Fig. 2.

The slight decrease in the O_{II} peak observed in (a) corresponds to the reduction in the Sn^{4+} peak observed in (b) and supports the case for Sn-O bonds as the source of the O_{II} peak [60–62]. For the film subject to a single ReLA pulse at 125 mJcm^{-2} in the reducing environment of 5% H_2 in N_2, the O_I peak is enhanced at the expense of the O_{II} peak, indicating that there is an enhancement of the crystalline order and a reduction of both Sn-O bonds. It is also found that the surface defects (O_{III} peak) are slightly reduced. There is also a corresponding activation of Sn^{4+} donors, partially explaining the increase in N_{opt} and N_{Hall} observed after laser processing. The concentration of oxygen vacancies cannot be reliably determined by de-convoluting the O1s XPS

Optical Materials EXPRESS

peak [25]. Therefore, we instead examine the abundance of oxygen relative to the abundance of the O1s, $In3d_{5/2}$ and $Sn3d_{5/2}$ peaks, where the individual peak areas were corrected by their respective relative sensitivity factors [65, 66].

The surface region O/(In + Sn) ratio is presented for the seed ITO film (grey bar) and that subject to single-pulse ReLA at 125 $mJcm^{-2}$ in 5% H_2 in N_2 (red bar) in Fig. 5(c). The O/(In + Sn) ratio is decreased by laser annealing, where the solid horizontal red line indicates the post-ReLA O/(In + Sn) ratio for an optimized ITO film [25]. The higher, more stoichiometric (dashed black line), concentration of oxygen likely corresponds to a smaller density of oxygen vacancies, explaining the other cause of the lower N for the ITO film of this work. The increase in the oxygen deficiency after ReLA correspondingly explains the increase in the carrier concentration (alongside Sn^{4+} activation). Significantly, the oxygen vacancy modulation is directly related to the ambient dependence modulation of the carrier concentration during ReLA. It is important to note that XPS is sensitive only to the surface of the thin film, such that we lose information on the observed depth-dependence of the ReLA process. Figure 5(c) is used to calibrate the EDX-calculated depth profile of the normalized O/(In + Sn) ratio across the sample depth for the seed ITO film (grey stars) and those subject to single-pulse ReLA at 12 $mJcm^{-2}$ in 5% H_2 in N_2 (red circles) and in 100% O_2 (green triangles). This is presentation as a function of the distance from the bottom of the film in Fig. 5(d). Note that the EDX results are offset so that the values of O/(In + Sn) for the seed and annealed film, at roughly 10 nm below the imaged surface (to account for the sampling depth [67]), match the values determined from XPS. Further details on the analysis of the EDX images is presented in Supplement 1, section 6. These steps allow us to examine how the oxygen content varies across the film. A gradient of the carrier concentration is observed throughout the depth of the film. The sharp increase of O/(In + Sn) at the bottom of the seed film may explain the existence of the bottom layer required to model the optical properties of the film. We note that the gradient in O/(In + Sn) is sharper for the film processed in 5% H_2 in N_2 than for the film processed in 100% O_2, and that near the surface there is a sharp dip in O/(In + Sn). From this, it is apparent that the reducing environment creates a steeper reduction of the oxygen across the depth of the film. This effect has been explained to arise from the promotion of oxygen mobility and Sn activation in response to the photo-induced localized heating [25].

6. Conclusions

Laser processing an "un-optimized", low-free carrier, seed ITO material within pressurized environments containing reducing and oxidizing reactive gasses was investigated in order to further reveal the physical mechanisms behind the conversion of the optical properties of ITO during ReLA. A complex interplay between the film structure, composition and optoelectronic behavior was revealed, building upon previous investigations of ITO and ReLA. Specifically, multiple charge species and a complex inhomogeneity were required to model the optical properties of ITO. By examining the carrier transport mechanisms of the two carrier species for the larger set of seed and laser processed films, considering the effect of various scattering mechanisms, the nature of the multiple carrier species was revealed. The two carrier species were found to arise from carriers that were scattered by ionized impurities and those that were scattered by grain boundaries or by clusters of defects that act like grain boundaries. This has implications for ITO films with lower carrier concentration used to target ENZ regions further into the IR. Furthermore, the modelling used to elucidate the dual carrier species could be investigated for a wider range of nano- and poly-crystalline materials.

Clear structural modifications occurred when laser processing at a high fluence (125 $mJcm^{-2}$). Specifically, the upper layer of the film became polycrystalline after ReLA. The depth dependence of the structural modifications was shown to arise from the change of the peak temperature across the film, due to the natural depth-dependence of the ReLA process. Despite the complexity of the

Optical Materials EXPRESS

structural modifications, it was found that the compositional modifications induced by ReLA were near-identical to previous reports. Specifically, the laser treatment induced both an activation of Sn dopants and a modification of the oxygen vacancy concentration throughout the depth of the film. The modulation of the oxygen vacancies was deemed to be the likely cause for the ambient dependent modulation of the carrier concentration and gave rise to the ability to tune the carrier concentration by controlling the mixture of oxidizing or reactive gasses within the pressure cell during ReLA. Hereby, we demonstrate how ReLA of low-N ITO films can tune the carrier concentration of ITO between $(0.3 - 1.27) \times 10^{20}$ cm^{-3} and modulate the ENZ wavelength of the top layer between 3.07 – 11.7 μm (with a single laser pulse) while simultaneously enhancing the figures of merit for SPP, LSPR, near-field enhancement and photothermal conversion. Vitally, the modulation range is significantly larger than has been reported for ReLA of high-N ITO films 1.91 – 1.73 μm [25], opening the mid-infrared spectral range for low-loss plasmonics and photonics.

Disclosures. The authors declare no conflicts of interest.

Data availability. Data underlying the results presented in this paper are not publicly available at this time but may be obtained from the corresponding author upon reasonable request.

Supplemental document. See Supplement 1 for supporting content.

References

1. D. S. Ginley, *Handbook of Transparent Conductors*, 1st ed. (Springer US, 2011).
2. Z. Wang, C. Chen, K. Wu, H. Chong, and H. Ye, "Transparent Conductive Oxides and Their Applications in Near Infrared Plasmonics," Phys. Status Solidi A **216**(5), 1700794 (2019).
3. L. Wang, J. Wen, C. Yang, and B. Xiong, "Potential of ITO thin film for electrical probe memory applications," Sci. Technol. Adv. Mater. **19**(1), 791–801 (2018).
4. J. Navarro-Arenas, J. Parra, and P. Sanchis, "Ultrafast all-optical phase switching enabled by epsilon-near-zero materials in silicon," Opt. Express **30**(9), 14518 (2022).
5. O. Reshef, I. de Leon, M. Z. Alam, and R. W. Boyd, "Nonlinear optical effects in epsilon-near-zero media," Nat. Rev. Mater. **4**(8), 535–551 (2019).
6. J. Wu, Z. T. Xie, Y. Sha, H. Y. Fu, and Q. Li, "Epsilon-near-zero photonics: infinite potentials," Photonics Res. **9**(8), 1616 (2021).
7. J. W. Kim, H. Kim, M. Y. Lee, D. Y. Lee, J. S. Lee, Y. H. Jang, J. S. Bae, J. S. Lee, and S. Park, "Atomistic aspects of carrier concentration variation in post-annealed indium tin oxide films," J. Phys. D: Appl. Phys. **48**(39), 395307 (2015).
8. R. X. Wang, C. D. Beling, S. Fung, A. B. Djurišic, C. C. Ling, and S. Li, "Influence of gaseous annealing environment on the properties of indium-tin-oxide thin films," J. Appl. Phys. **97**(3), 033504 (2005).
9. Y. Hu, X. Diao, C. Wang, W. Hao, and T. Wang, "Effects of heat treatment on properties of ITO films prepared by rf magnetron sputtering," Vacuum **75**(2), 183–188 (2004).
10. W. Jaffray, S. Saha, V. M. Shalaev, A. Boltasseva, and M. Ferrera, "Transparent conducting oxides: from all-dielectric plasmonics to a new paradigm in integrated photonics," Adv. Opt. Photonics **14**(2), 148 (2022).
11. S. Lal, S. Link, and N. J. Halas, "Nano-optics from sensing to waveguiding," Nat. Photonics **1**(11), 641–648 (2007).
12. J. Martínez, A. Ródenas, M. Aguiló, T. Fernandez, J. Solis, and F. Díaz, "Mid-infrared surface plasmon polariton chemical sensing on fiber-coupled ITO coated glass," Opt. Lett. **41**(11), 2493 (2016).
13. G. V. Naik, V. M. Shalaev, and A. Boltasseva, "Alternative Plasmonic Materials: Beyond Gold and Silver," Adv. Mater. **25**(24), 3264–3294 (2013).
14. J. D. Caldwell, L. Lindsay, V. Giannini, I. Vurgaftman, T. L. Reinecke, S. A. Maier, and O. J. Glembocki, "Low-loss, infrared and terahertz nanophotonics using surface phonon polaritons," Nanophotonics **4**(1), 44–68 (2015).
15. A. Lalisse, G. Tessier, J. Plain, and G. Baffou, "Quantifying the Efficiency of Plasmonic Materials for Near-Field Enhancement and Photothermal Conversion," J. Phys. Chem. C **119**(45), 25518–25528 (2015).
16. P. Berini, "Figures of merit for surface plasmon waveguides," Opt. Express **14**(26), 13030 (2006).
17. J. B. Khurgin, "Relative merits of phononics vs. plasmonics: the energy balance approach," Nanophotonics **7**(1), 305–316 (2018).
18. U. Guler, V. M. Shalaev, and A. Boltasseva, "Nanoparticle plasmonics: going practical with transition metal nitrides," Mater. Today **18**(4), 227–237 (2015).
19. A. Manjavacas, J. G. Liu, V. Kulkarni, and P. Nordlander, "Plasmon-Induced Hot Carriers in Metallic Nanoparticles," ACS Nano **8**(8), 7630–7638 (2014).
20. F. Wang and Y. R. Shen, "General Properties of Local Plasmons in Metal Nanostructures," Phys. Rev. Lett. **97**(20), 206806 (2006).
21. C.-S. Huang and C.-C. Liu, "The optical and electrical properties of gallium-doped ZnO thin film with post-annealing processes of various atmospheres," Microelectron. Eng. **148**, 59–63 (2015).

Optical Materials EXPRESS

22. Y. Wang, A. Capretti, and L. Dal Negro, "Wide tuning of the optical and structural properties of alternative plasmonic materials," Opt. Mater. Express **5**(11), 2415 (2015).
23. R.-H. Horng, S.-L. Ou, C.-Y. Huang, P. Ravadgar, and C.-I. Wu, "Effects of Ga concentration and rapid thermal annealing on the structural, optoelectronic and photoluminescence properties of Ga-doped ZnO thin films," Thin Solid Films **605**, 30–36 (2016).
24. E. Yarali, C. Koutsiaki, H. Faber, K. Tetzner, E. Yengel, P. Patsalas, N. Kalfagiannis, D. C. Koutsogeorgis, and T. D. Anthopoulos, "Recent Progress in Photonic Processing of Metal-Oxide Transistors," Adv. Funct. Mater. **30**(20), 1906022 (2020).
25. J. A. Hillier, P. Patsalas, D. Karfaridis, S. Camelio, W. Cranton, A. V. Nabok, C. J. Mellor, D. C. Koutsogeorgis, and N. Kalfagiannis, "Photo-Engineered Optoelectronic Properties of Indium Tin Oxide via Reactive Laser Annealing," Scientific Reports, submitted for publication (2022). Preprint available at Research Square: https://doi.org/10.21203/rs.3.rs-1752808/v1.
26. J. A. Hillier, "Photo-engineered Optoelectronic Properties of Transparent Conductive Oxides via Reactive Laser Annealing (ReLA): The Consequence of Defects.," Doctoral dissertation, Nottingham Trent University (2021).
27. S. O. El Hamali, W. M. Cranton, N. Kalfagiannis, X. Hou, R. Ranson, and D. C. Koutsogeorgis, "Enhanced electrical and optical properties of room temperature deposited Aluminium doped Zinc Oxide (AZO) thin films by excimer laser annealing," Optics and Lasers in Engineering **80**, 45–51 (2016).
28. H. G. Tompkins and J. N. Hilfiker, *Spectroscopic Ellipsometry Practical Application to Thin Film Characterization* (Momentum Press, 2016).
29. W. Seiler, M. Nistor, C. Hebert, and J. Perrière, "Epitaxial undoped indium oxide thin films: Structural and physical properties," Solar Energy Materials and Solar Cells **116**, 34–42 (2013).
30. J. Gao, K. Kempa, M. Giersig, E. M. Akinoglu, B. Han, and R. Li, "Physics of transparent conductors," Adv. Phys. **65**(6), 553–617 (2016).
31. G. Gonçalves, E. Elangovan, P. Barquinha, L. Pereira, R. Martins, and E. Fortunato, "Influence of post-annealing temperature on the properties exhibited by ITO, IZO and GZO thin films," Thin Solid Films **515**(24), 8562–8566 (2007).
32. J. A. Hillier, S. Camelio, W. Cranton, A. V. Nabok, C. J. Mellor, D. C. Koutsogeorgis, and N. Kalfagiannis, "When Ellipsometry Works Best: A Case Study With Transparent Conductive Oxides," ACS Photonics **7**(10), 2692–2702 (2020).
33. A. Tamanai, T. D. Dao, M. Sendner, T. Nagao, and A. Pucci, "Mid-infrared optical and electrical properties of indium tin oxide films," Phys. Status Solidi A **214**(3), 1600467 (2017).
34. G. E. Jellison and F. A. Modine, "Parameterization of the optical functions of amorphous materials in the interband region," Appl. Phys. Lett. **69**(3), 371–373 (1996).
35. S. Zollner, P. P. Paradis, F. Abadizaman, and N. S. Samarasingha, "Drude and Kukharskii mobility of doped semiconductors extracted from Fourier-transform infrared ellipsometry spectra," J. Vac. Sci. Technol., B: Nanotechnol. Microelectron.: Mater., Process., Meas., Phenom. **37**(1), 012904 (2019).
36. M. Feneberg, J. Nixdorf, C. Lidig, R. Goldhahn, Z. Galazka, O. Bierwagen, and J. S. Speck, "Many-electron effects on the dielectric function of cubic In2 O3: Effective electron mass, band nonparabolicity, band gap renormalization, and Burstein-Moss shift," Phys. Rev. B **93**(4), 045203 (2016).
37. P. Uprety, M. M. Junda, H. Salmon, and N. J. Podraza, "Understanding near infrared absorption in tin doped indium oxide thin films," J. Phys. D: Appl. Phys. **51**(29), 295302 (2018).
38. T. E. Tiwald, D. W. Thompson, J. A. Woollam, W. Paulson, and R. Hance, "Application of IR variable angle spectroscopic ellipsometry to the determination of free carrier concentration depth profiles," Thin Solid Films **313-314**, 661–666 (1998).
39. T. Pisarkiewicz and A. Kolodziej, "Nonparabolicity of the Conduction Band Structure in Degenerate Tin Dioxide," phys. stat. sol. (b) **158**(1), K5–K8 (1990).
40. K. Zhang, F. Zhu, C. H. A. Huan, and A. T. S. Wee, "Indium tin oxide films prepared by radio frequency magnetron sputtering method at a low processing temperature," Thin Solid Films **376**(1-2), 255–263 (2000).
41. K. Ellmer and R. Mientus, "Carrier transport in polycrystalline transparent conductive oxides: A comparative study of zinc oxide and indium oxide," Thin Solid Films **516**(14), 4620–4627 (2008).
42. K. Ellmer and R. Mientus, "Carrier transport in polycrystalline ITO and ZnO:Al II: The influence of grain barriers and boundaries," Thin Solid Films **516**(17), 5829–5835 (2008).
43. O. Bierwagen and J. S. Speck, "High electron mobility In2O3(001) and (111) thin films with nondegenerate electron concentration," Appl. Phys. Lett. **97**(7), 072103 (2010).
44. T. Koida and M. Kondo, "High electron mobility of indium oxide grown on yttria-stabilized zirconia," J. Appl. Phys. **99**(12), 123703 (2006).
45. M. V. Frischbier, H. F. Wardenga, M. Weidner, O. Bierwagen, J. Jia, Y. Shigesato, and A. Klein, "Influence of dopant species and concentration on grain boundary scattering in degenerately doped In2O3 thin films," Thin Solid Films **614**, 62–68 (2016).
46. J. W. Bae, S. D. Park, N. G. Cho, D. H. Lee, and G. Y. Yeom, "Effects of tin concentration on the electrical properties of room-temperature ion-beam-assisted-evaporation-deposited indium oxide thin films," Jpn. J. Appl. Phys. **41**(Part 2, No. 9A/B), L999–L1001 (2002).

Optical Materials EXPRESS

47. Y. Shigesato and D. C. Paine, "Study of the effect of Sn doping on the electronic transport properties of thin film indium oxide," Appl. Phys. Lett. **62**(11), 1268–1270 (1993).
48. F. Mei, T. Yuan, R. Li, K. Qin, and J. Huang, "Microstructure evolution and grain orientation in ITO targets and their effects on the film characteristics," J. Mater. Sci.: Mater. Electron. **29**(17), 14620–14634 (2018).
49. H. Hosono, M. Yasukawa, and H. Kawazoe, "Novel oxide amorphous semiconductors: transparent conducting amorphous oxides," J. Non-Cryst. Solids **203**, 334–344 (1996).
50. H. Hosono, N. Kikuchi, N. Ueda, and H. Kawazoe, "Working hypothesis to explore novel wide band gap electrically conducting amorphous oxides and examples," J. Non-Cryst. Solids **198-200**, 165–169 (1996).
51. J. Y. W. Seto, "The electrical properties of polycrystalline silicon films," J. Appl. Phys. **46**(12), 5247–5254 (1975).
52. G. Frank and H. Köstlin, "Electrical properties and defect model of tin-doped indium oxide layers," Appl. Phys. A **27**(4), 197–206 (1982).
53. Y. Kudo, K. Kawabata, and H. Goto, "A possibility for generation of two species of charge carriers along main-chain and side-chains for a π-conjugated polymer," J. Phys.: Conf. Ser. **428**, 012006 (2013).
54. G. Giusti, "Deposition and Characterisation of Functional Ito Thin Films," Doctoral dissertation, University of Birmingham (2011).
55. J. B. Khurgin and A. Boltasseva, "Reflecting upon the losses in plasmonics and metamaterials," MRS Bull. **37**(8), 768–779 (2012).
56. F. Khalilzadeh-Rezaie, I. O. Oladeji, J. W. Cleary, N. Nader, J. Nath, I. Rezadad, and R. E. Peale, "Fluorine-doped tin oxides for mid-infrared plasmonics," Opt. Mater. Express **5**(10), 2184 (2015).
57. F. Mei, T. Yuan, and R. Li, "Effects of second-phase particles and elemental distributions of ITO targets on the properties of deposited ITO films," Ceram. Int. **43**(12), 8866–8872 (2017).
58. A. Bouhdjer, H. Saidi, A. Attaf, A. Yahia, M. S. Aida, O. Benkhetta, and L. Bouhdjer, "Effects of lattice mismatches in In2O3/substrate structures on the structural, morphological and electrical properties of In2O3 films," Surf. Interfaces **20**, 100579 (2020).
59. D. Mergel, M. Schenkel, M. Ghebre, and M. Sulkowski, "Structural and electrical properties of In2O3:Sn films prepared by radio-frequency sputtering," Thin Solid Films **392**(1), 91–97 (2001).
60. J. S. Kim, P. K. H. Ho, D. S. Thomas, R. H. Friend, F. Cacialli, G.-W. Bao, and S. F. Y. Li, "X-ray photoelectron spectroscopy of surface-treated indium-tin oxide thin films," Chem. Phys. Lett. **315**(5-6), 307–312 (1999).
61. J. C. C. Fan and J. B. Goodenough, "X-ray photoemission spectroscopy studies of Sn-doped indium-oxide films," J. Appl. Phys. **48**(8), 3524–3531 (1977).
62. N. Mori, S. Ooki, N. Masubuchi, A. Tanaka, M. Kogoma, and T. Ito, "Effects of postannealing in ozone environment on opto-electrical properties of Sn-doped In2O3 thin films," Thin Solid Films **411**(1), 6–11 (2002).
63. J. H. Park, C. Buurma, S. Sivananthan, R. Kodama, W. Gao, and T. A. Gessert, "The effect of post-annealing on Indium Tin Oxide thin films by magnetron sputtering method," Appl. Surf. Sci. **307**, 388–392 (2014).
64. H. J. Kim, M. J. Maeng, J. H. Park, M. G. Kang, C. Y. Kang, Y. Park, and Y. J. Chang, "Chemical and structural analysis of low-temperature excimer-laser annealing in indium-tin oxide sol-gel films," Current Applied Physics **19**(2), 168–173 (2019).
65. C. D. Wagner, "Sensitivity factors for XPS analysis of surface atoms," J. Electron Spectrosc. Relat. Phenom. **32**(2), 99–102 (1983).
66. C. J. Powell, "Recommended Auger parameters for 42 elemental solids," J. Electron Spectrosc. Relat. Phenom. **185**(1-2), 1–3 (2012).
67. C. J. Powell and A. Jablonski, "Progress in quantitative surface analysis by X-ray photoelectron spectroscopy: Current status and perspectives," J. Electron Spectrosc. Relat. Phenom. **178-179**, 331–346 (2010).